

Sr-induced dipole scatter in BST: Insights from MD simulations using a transferable bond valence-based interatomic potential

Robert B. Wexler,¹ Yubo Qi,² and Andrew M. Rappe¹

¹*Department of Chemistry, University of Pennsylvania,
Philadelphia, Pennsylvania 19104, USA*

²*Department of Physics and Astronomy,
Rutgers University, Piscataway, New Jersey 08854, USA*

(Dated: May 31, 2019)

Abstract

In order to design next-generation ferroelectrics, a microscopic understanding of their macroscopic properties is critical. One means to achieving an atomistic description of ferroelectric and dielectric phenomena is classical molecular dynamics simulations. Previously, we have shown that interatomic potentials based on the bond valence molecular dynamics (BVMD) method can be used to study structural phase transitions, ferroelectric domain nucleation, and domain wall migration in several perovskite oxides and fixed-composition binary and ternary alloys. Most modern devices, however, use variable-composition perovskite oxide alloys such as $\text{Ba}_x\text{Sr}_{1-x}\text{TiO}_3$ (BST). In this paper, we extend our bond valence approach to BST solid solutions and, in so doing, show that the potential parameters for each element are transferable between materials with different x . Using this potential, we perform BVMD simulations investigating the temperature and composition dependence of the lattice constants, Ti displacements, and ferroelectric polarization of BST and find that our predictions match experiments and first-principles theory. Additionally, based on a detailed analysis of local dipole distributions, we demonstrate that substitution of Sr for Ba scrambles dipoles, reduces global polarization, and enhances the order-disorder character of the ferroelectric-paraelectric phase transition.

I. INTRODUCTION

Bond valence-based interatomic potentials have proven to be a powerful tool, enabling fast and large-scale molecular dynamics (MD) simulations of ferroelectric oxides. Interatomic potentials for several technologically important perovskite materials, such as BaTiO_3 , PbTiO_3 , PbZrO_3 and BiFeO_3 have been successfully developed.¹⁻⁶ In addition, bond-valence MD (BVMD) potentials successfully describe PZT $\text{Pb}(\text{Zr}_{0.5}\text{Ti}_{0.5})\text{O}_3$ and 25% PMN-PT $\text{Pb}(\text{Mg}_{0.25}\text{Ti}_{0.25}\text{Nb}_{0.5})\text{O}_3$, single-composition binary and ternary alloys.¹⁻¹¹ In these potentials, however, the parameters corresponding to a specific element are material-dependent, not just species-dependent. For example, the fitted Coulombic charges for oxygen are different in each material, which makes BVMD simulations for arbitrary x of $(A_x A'_{1-x})\text{BO}_3$ or $A(B_x B'_{1-x})\text{O}_3$ alloys impossible. Given this limitation, we aim to develop transferable interatomic potentials where the parameters corresponding to a particular element depend only on that element's intrinsic properties and, therefore, can be used for different materials and their heterostructures and alloys with diverse chemical compositions. In this paper, we report the successful development of a transferable interatomic potential for $\text{Ba}_x\text{Sr}_{1-x}\text{TiO}_3$ (BST). BVMD simulations using this potential accurately reproduce the experimentally determined temperature-composition phase diagram of BST. Additionally, the atomistic nature of our interatomic potential enables analysis of local dipole distributions, which reveal that the substitution of Sr for Ba weakens the correlation between and promotes arbitrarily-oriented Ti displacements, suppresses the global polarization, and changes the character of the ferroelectric-paraelectric phase transition. This work not only presents proof of concept for the development of element-dependent, transferable BVMD interatomic potentials but also provides atomistic insights into the relationship between the thermodynamic properties of BST and its composition.

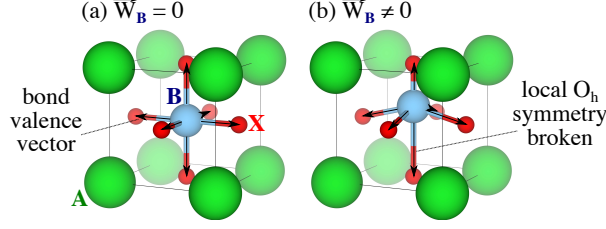


FIG. 1. Bond valence vector sum (BVVS) of (a) a centrosymmetric perovskite structure with zero BVVS and (b) a polar perovskite structure with non-zero BVVS. The Ba, Ti, and O atoms are represented by green, blue, and red spheres respectively.

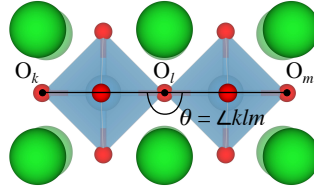


FIG. 2. Schematic representation of the angle potential.

II. COMPUTATIONAL METHODS

A. Bond valence-based interatomic potentials

In the bond valence model, the valence of a bond (V_{ij}) between atoms i and j is defined as the number of electron pairs used to form that bond and is expressed mathematically as

$$V_{ij} = \left(\frac{r_{0,ij}}{r_{ij}} \right)^{C_{ij}} \quad (1)$$

where $r_{0,ij}$ is a reference distance between atoms i and j , r_{ij} is the instantaneous distance, and C_{ij} is an empirical parameter related to the force constant of the chemical bond.^{2,4-7,12-15} The valence of an atom i (V_i) is obtained by summing the bond valences of the bonds it forms with its neighbors j ,

$$V_i = \sum_j^{N_n} V_{ij}, \quad (2)$$

where N_n is the number of neighbors. Due to the bond valence conservation principle, there is an energy penalty (E_{BV}) if the atomic valence deviates from its optimal value ($V_{0,i}$)

$$E_{BV} = \sum_i^{N_a} S_i (V_i - V_{0,i})^2 \quad (3)$$

where N_a is the number of atoms in the unit cell and S_i is a scaling factor. Chemically speaking, E_{BV} describes the energy increase associated with over- and under-coordination of atoms.

The bond valence vector is defined as $\vec{V}_{ij} = V_{ij}\hat{R}_{ij}$ where \hat{R}_{ij} is the unit vector pointing from atom i to atom j . The sum of the bond valence vectors of an atom i

$$\vec{W}_i = \sum_j^{N_n} \vec{V}_{ij} \quad (4)$$

is a measure of local symmetry breaking. Take, for example, the perovskite ABX_3 structure shown in Figure 1. In Figure 1(a), the B -site cation sits at the center of an octahedral cage of X anions. In this arrangement, the B - X bond valence vectors cancel, yielding $\vec{W}_B = 0$. If the B -site cation displaces off-center, as in Figure 1(b), the bond valence vectors along the displacement direction no longer cancel, leading to a non-zero \vec{W}_B . Similar to Equation 3, a bond valence vector energy (E_{BVV}) can be written as

$$E_{\text{BVV}} = \sum_i^{N_a} D_i \left(\vec{W}_i^2 - \vec{W}_{0,i}^2 \right)^2 \quad (5)$$

where D_i is a scaling factor and $|\vec{W}_{0,i}|$ is the preferred bond valence vector length. This energy term is important for capturing the equilibrium off-center displacements of ions ($\vec{W}_{0,i} \neq 0$) in ferroelectric materials. Previously, we have shown that E_{BV} and E_{BVV} are equivalent to second- and fourth-moment bond order potentials, respectively.¹⁶ This equivalence shows that Equations 3 and 5 have a quantum mechanical foundation.^{4,5,15,17,18}

In our scheme, the total energy of the system is given by

$$E = E_{\text{BV}} + E_{\text{BVV}} + E_r + E_c + E_a \quad (6)$$

$$E_r = \sum_{i < j} \left(\frac{B_{ij}}{r_{ij}} \right)^{12} \quad (7)$$

$$E_c = \sum_{i < j} \frac{q_i q_j}{r_{ij}} \quad (8)$$

$$E_a = k \sum_i (\theta_i - 180^\circ)^2 \quad (9)$$

where E_r is the short-range repulsion energy, E_c is the Coulomb energy, E_a is the X_6 octahedral tilting energy, B_{ij} is the short-range repulsion parameter, q is the charge in units

	$r_{0,\beta\text{O}}$	$C_{0,\beta\text{O}}$	q_β (e)	S_β (eV)	D_β	$B_{\beta\beta'}$ (Å)				$V_{0,\beta}$	$\vec{W}_{0,\beta}$
						Ba	Sr	Ti	O		
Ba	2.290	8.94	1.34730	0.59739	0.08429	2.44805	2.40435	2.32592	1.98792	2.0	0.11561
Sr	2.143	8.94	1.34730	0.63624	9.99121		0.38947	1.68014	1.96311	2.0	0.00000
Ti	1.798	5.20	1.28905	0.16533	0.82484			2.73825	1.37741	4.0	0.39437
O			-0.87878	0.93063	0.28006				1.99269	2.0	0.31651

TABLE I. Optimized parameters of the bond valence-based interatomic potential for BST. The scaling constant k is $0.0609 \text{ eV}/(\text{deg})^2$.

of $|e|$, k is a scaling factor, and θ_i is the octahedral tilting angle (see Figure 2) in degrees calculated as $\angle klm$.

Bond valence-based interatomic potentials enable efficient, large-scale MD simulations and have been used successfully in the past to study structural phase transitions,¹⁻⁶ the nucleation of ferroelectric domains,¹⁹⁻²¹ the dynamics of the walls separating these domains in perovskites,²⁰ and relaxor ferroelectrics.⁸⁻¹¹ For this reason, we have developed interatomic potentials for several technologically important perovskites such as PbTiO_3 ,^{1-3,5,21} BiFeO_3 ,^{4,22,23} PbZrO_3 , BaTiO_3 (BTO),⁶ PZT,^{1,7} and PMN-PT.⁸⁻¹¹ Based on these successes, we extend this approach to include the perovskite alloy family BST. We note that our previously developed interatomic potential for BTO accurately reproduces many physical properties such as lattice constants, permittivities, and the structural phase transition sequence. Therefore, the parameters related to Ba, Ti, and O elements are kept fixed, and only those related to Sr ($r_{0,\text{SrO}}$, C_{SrO} , S_{Sr} , D_{Sr} , and B_{SrX} where $X \in \{\text{Ba}, \text{Sr}, \text{Ti}, \text{O}\}$) were optimized. Additionally, in order to maintain charge neutrality, we set the charge of Sr equal to that of Ba.

B. Parameterization

The parameters of the interatomic potential were fit to reproduce density functional theory (DFT)^{24,25} calculations of BST using an optimization protocol described elsewhere.⁵ DFT calculations were carried out using the QUANTUM ESPRESSO software package.²⁶ Designed,²⁷ optimized, norm-conserving pseudopotentials²⁸ were used to replace the core

electrons with a smoother, effective potential. The exchange-correlation contribution to the total energy was calculated using the PBEsol functional, which was designed specifically for bulk solids and provides excellent agreement with the experimental lattice parameters and spontaneous polarization of BTO.²⁹ The electronic wave functions were expanded in a plane-wave basis set with an energy cutoff of 60 Ry. Integrals over the Brillouin zone were evaluated using a Γ -centered, $4\times 4\times 4$ k -point mesh. Our database consists of 612 structures extracted from variable-cell relaxations; every structure is a $2\times 2\times 2$ supercell containing 40 atoms. The total energy, force, and pressure convergence criteria for these relaxations were 1.4×10^{-5} eV/supercell, 2.7×10^{-4} eV/Å, and 0.5 kbar, respectively. For self-consistent field calculations, the total energy convergence threshold was 1.4×10^{-8} eV/supercell. The average absolute difference between the DFT and MD energies is 1.12×10^{-3} eV/atom. The optimized parameters are listed in Table I.

C. Molecular dynamics simulations

MD simulations were performed using an in-house version of the Large-scale Atomic Molecular Massively Parallel Simulator (LAMMPS)³⁰ that was modified to calculate the bond valence and bond valence vector energies. We investigated five different concentrations of Sr in BST: 10%, 30%, 50%, 70%, and 90%. For each concentration, Ba was replaced with Sr randomly. Every structure is a $20\times 20\times 20$ supercell containing 40,000 atoms. We find this to be more than sufficient (only $10\times 10\times 10$ is necessary) to converge the structural phase transition sequence of $\text{Ba}_{0.9}\text{Sr}_{0.1}\text{TiO}_3$ (see Figure S1 in the Supplemental Material). Long-range Coulombic interactions were computed using the particle-particle particle-mesh solver with a desired absolute error in the forces of 1×10^{-4} eV/Å. The cutoff distance for short-range interactions was chosen to be 8 Å. Neighbor lists, containing all atom pairs within 10 Å, were updated every step. The time step for MD simulations was 1 fs. We studied temperatures ranging from 10 K to 170 K. For each temperature, the simulation consisted of three steps: (1) *NVT* equilibration, (2) *NPT* equilibration, and (3) *NPT* sampling. The first step runs for 10 ps and generates positions and velocities sampled from the canonical ensemble using the Nosé-Hoover thermostat³¹⁻³³ with a temperature damping parameter of 1 ps. The second step relaxes the volume constraint to sample from the isothermal-isobaric ensemble for 40 ps at 1.01325 bar using the Parrinello-Rahman barostat^{34,35} with a pressure

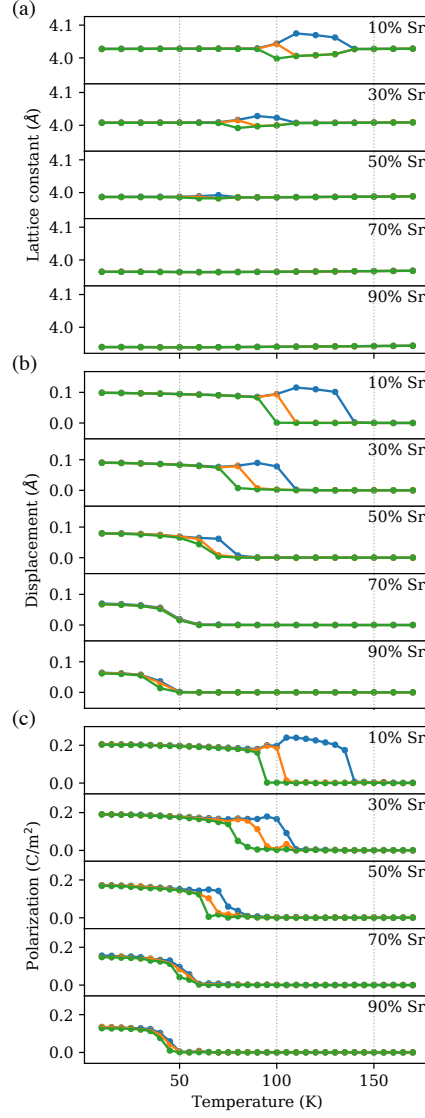


FIG. 3. Temperature dependence of the (a) lattice constants, (b) Ti displacements, and (c) polarization components of BST for different compositions.

damping parameter of 5 ps. The third step samples the NPT -equilibrated structure for 40 ps, from which thermodynamic time averages can be computed.

III. RESULTS AND DISCUSSION

A. Thermodynamic properties of BST

We tested the performance of the interatomic potential for BST by calculating the lattice constants, components of the Ti displacements, and components of the polarization as a function of the temperature and concentration of Sr. Figure 3(a) shows how the lattice constants change as BST is heated from low to high temperature. For 10% Sr, the evolution of the lattice constants is very similar to that of BTO. It is well-known experimentally that BTO undergoes three structural phase transitions: (1) from rhombohedral ($P \parallel [111]$) to orthorhombic ($P \parallel [110]$), (2) from orthorhombic to tetragonal ($P \parallel [100]$), and (3) from tetragonal to cubic ($P = 0$).³⁶⁻³⁸ First, we will discuss BST with 10% Sr. At temperatures less than or equal to 90 K, a rhombohedral phase is preferred. Between 90 K and 110 K, BST becomes orthorhombic. From 110 K to 140 K, the system favors a tetragonal crystal structure. Finally, at 140 K, a tetragonal to cubic phase transition occurs. The rhombohedral to orthorhombic to tetragonal to cubic phase transition sequence is in excellent qualitative agreement with experiments and other computational studies.³⁶⁻⁴¹ The phase transition temperatures, however, are underestimated, and this is likely due to the fact that DFT underestimates the energy differences between these four structural phases. This hypothesis is supported by the fact that other theoretical models based on DFT also give phase transition temperatures that are too low.³⁹⁻⁴² As the concentration of Sr is increased, the rhombohedral-orthorhombic and tetragonal-cubic phase transition temperatures decrease, and the orthorhombic and tetragonal phases disappear at and above 70% Sr, both of which are seen experimentally.³⁶⁻³⁸ Additionally, we find that the lattice constants of BST decrease with increasing Sr content because the ionic radius of Sr (1.44 Å) is smaller than that of Ba (1.61 Å).

In addition to the crystal lattice, the position of Ti relative to the center of its O_6 octahedral cage also depends on the temperature and composition of BST, as shown in Figure 3(b). There are four possible displacement modes of Ti: $[111]$, $[110]$, $[100]$, and $[000]$, where the last corresponds to Ti at the center of the octahedron. The transition temperatures for the Ti displacements are the same as those for the structural phase transitions so they will not be repeated here. For 10% and 30% Sr, three different displacement transitions

are observed: (1) from [111] to [110], (2) from [110] to [100], and (3) from [100] to [000], ranked from the lowest to highest transition temperature. This ordering is the same as that of BTO and is consistent with experimental measurements of the Ti displacement.³⁷ The magnitude of the Ti displacement decreases as more Sr is introduced into the system because the shrinking of the lattice reduces the room for Ti to move off-center.

We also analyzed the effect of temperature and Sr concentration on the polarization of BST. The polarization plotted in Figure 3(c) is calculated as

$$\vec{P}(t) = \frac{1}{N_u} \sum_i^{N_u} \vec{P}_i(t) \quad (10)$$

where t is time, N_u is the number of unit cells, and P_i is the polarization of unit cell i

$$\vec{P}_i(t) = \frac{1}{\Omega_i} \left(\frac{1}{8} \sum_{j=1}^8 \mathbf{Z}_A^* \vec{r}_{A,j}(t) + \mathbf{Z}_{\text{Ti}}^* \vec{r}_{\text{Ti}}(t) + \frac{1}{2} \mathbf{Z}_O^* \cdot \sum_{j=1}^6 \vec{r}_{O,j}(t) \right) \quad (11)$$

where Ω is the volume of the unit cell, \mathbf{Z}^* are the Born effective charge tensors (taken from Reference 43), A is either Ba or Sr, and \vec{r} is the position of each atom relative to the center of the unit cell. Here, we define a unit cell as having eight A -site cations at the corners, one Ti at the center, and six O at the face centers. The temperature profile of the polarization components is very similar to that of the Ti displacements. For Sr concentrations less than 30%, the direction of the polarization changes from [111] to [110] to [100] to [000]. The last change is a ferroelectric to paraelectric phase transition that occurs at the Curie temperature (T_C). Increasing the amount of Sr reduces the T_C substantially, which is in excellent agreement with the experimental literature on BST.³⁶⁻³⁸ The magnitude of the [111] polarization for 10% Sr (0.35 C/m²) also matches previous experimental (0.31 C/m²)³⁷ and computational (0.16 C/m² and 0.44 C/m²)^{39,41} reports.

B. Temperature-composition phase diagram

As a next step in validating our interatomic potential, we construct the temperature-composition phase diagram of BST and compare it with experiments. The phase diagram is shown in Figure 4, where the rhombohedral, orthorhombic, tetragonal, and cubic phases are shaded red, orange, blue, and green, respectively. We are able to reproduce two key features of the phase diagram: (1) the shifts of the ferroelectric-paraelectric and ferroelectric-ferroelectric phase transition lines to lower temperature with increasing Sr concentration and

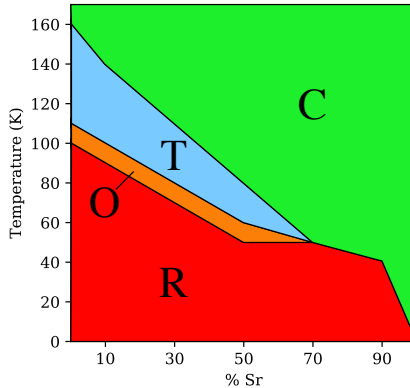


FIG. 4. Temperature-composition phase diagram of BST. Red, orange, blue, and green correspond to the rhombohedral, orthorhombic, tetragonal, and cubic phases.

(2) the presence of a tricritical point (TCP) near 70% Sr. It has been shown that, at the TCP, the character of the ferroelectric-paraelectric phase transition goes from first-order to second-order.^{36,38} This can be seen in Figure 3(c) where, between 50% Sr and 70% Sr, the transition from non-zero to zero polarization becomes less sharp.

C. Effects of Sr substitution on dipolar structure

The strong agreement between BVMD and experimental phase diagrams indicates that this BVMD interatomic potential for BST is accurate and can be used to explore the atomistic origins of structural phase transitions in solid solutions. In order to investigate changes in local physicochemical properties with Sr substitution, we examine the temperature dependence of the Ti displacement distributions of Ba-rich BST ($\text{Ba}_{0.9}\text{Sr}_{0.1}\text{TiO}_3$, see Figures 5(a) and (b)) and Sr-rich BST ($\text{Ba}_{0.1}\text{Sr}_{0.9}\text{TiO}_3$, see Figures 5(c) and (d)). Figure 5(a) shows that, for Ba-rich BST, the absolute values of the Ti displacements $|d_{\text{Ti}}|$ are normally distributed at all temperatures except at 10 K where two peaks are observed. The larger peak at 0.17 Å corresponds to the displacement of Ti atoms that are completely surrounded by Ba at the *A*-sites. The smaller peak at 0.20 Å, however, originates from Ti atoms whose neighboring *A*-sites are partially occupied by Sr.³⁹ The effect of Sr on $|d_{\text{Ti}}|$ can be seen more clearly in Figure 6(a), where the distribution of $|P_i|$ is plotted against the number of Sr in a Ti-centered cell (n_{Sr}). Each Ti has eight nearest neighbor *A*-sites and each of these can host either Ba or Sr. Consequently, we define n_{Sr} as the number of Sr occupying nearest neighbor

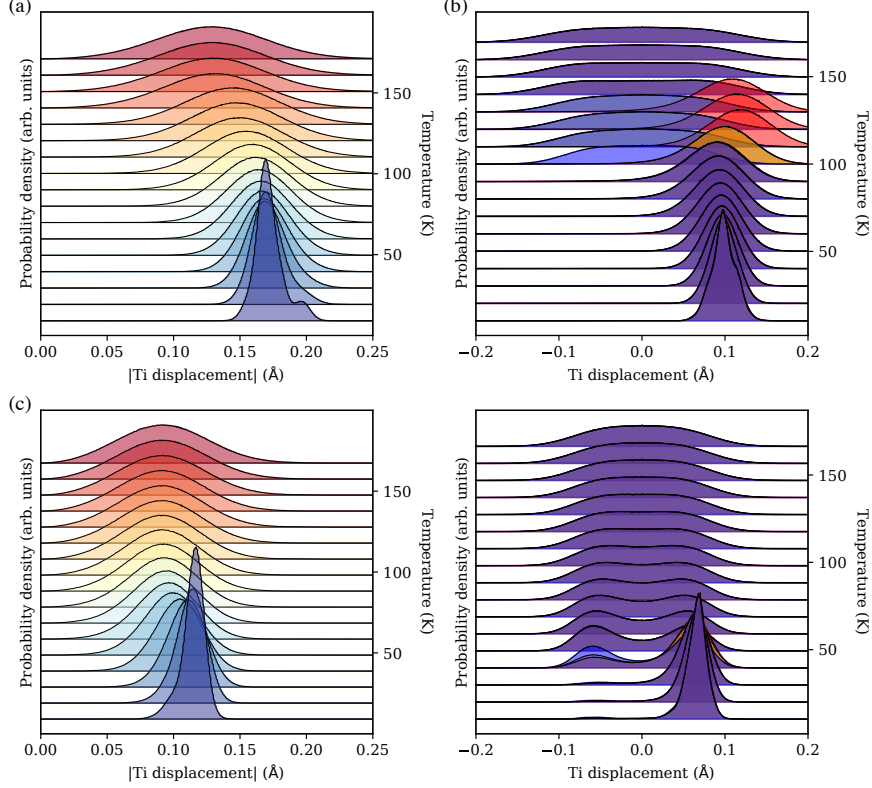


FIG. 5. Temperature dependence of (a) $|d_{\text{Ti}}|$ distributions and (b) Ti displacement distributions in three Cartesian directions for $\text{Ba}_{0.9}\text{Sr}_{0.1}\text{TiO}_3$. Those for $\text{Ba}_{0.1}\text{Sr}_{0.9}\text{TiO}_3$ are shown in (c) and (d), respectively. The colors in (a) and (c) correspond to the temperature of the simulation, blue being the coldest (10 K) and red the hottest (170 K). The colors in (b) and (d) correspond to the components of the Ti displacement in the three Cartesian directions: x is red, y is yellow, and z is blue. If some or all of these distributions overlap, then the resulting color is additive, *e.g.* red + yellow = orange.

A -sites for a particular Ti. We find that as n_{Sr} increases from 0 to 4, the median $|P_i|$ (shown as white points in Figure 6(a)) increases from 0.350 C/m^2 to 0.378 C/m^2 . The reason for the increased Ti displacement near Sr is that, for low Sr doping concentrations, the lattice constant does not change, but Sr takes up less volume than Ba. Therefore, the free volume available for off-center Ti displacements is larger when Sr is adjacent. The magnitude of this effect also depends on the position of Sr relative to that of Ti. If Ti is polarized along $[111]$, then there are four unique A -sites (see Figure 6(b)). Figure 6(c) shows that, for $n_{\text{Sr}} = 1$, as the distance between Sr and Ti increases, the median $|P_i|$ decreases from 0.363 C/m^2 to 0.347 C/m^2 . This suggests that the free volume created by replacing Ba with

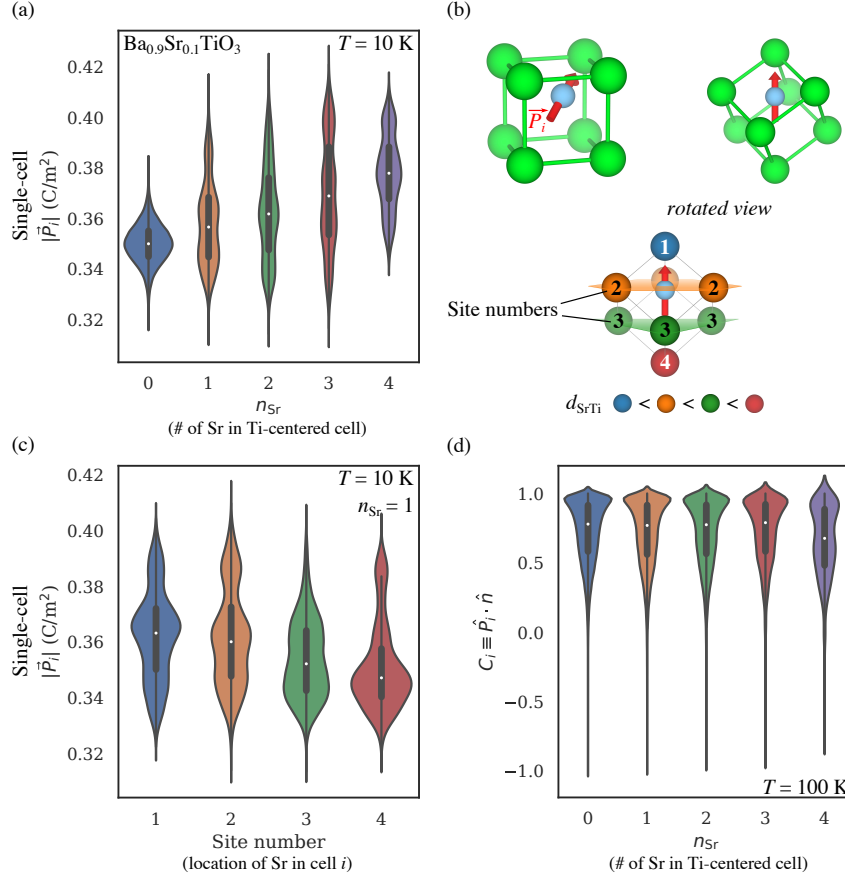


FIG. 6. The role of Sr dopants enhancing low- T polarization in $\text{Ba}_{0.9}\text{Sr}_{0.1}\text{TiO}_3$. (a) Dependence of $|P_i|$ on n_{Sr} at 10 K. We use a kernel density estimation of the underlying distribution. The bottom and top of the black rectangle correspond to the first and third quartiles, respectively. White points correspond to the median $|P_i|$. (b) The top shows the eight nearest-neighbor A -sites. The bottom shows the four unique A -sites for [111] polarized Ti. (c) Dependence of $|P_i|$ on the site number of the A -site occupied by Sr for $n_{\text{Sr}} = 1$. Numbering corresponds to the bottom of (b). (d) Dependence of the orientational correlation between dipoles, calculated as $C_i \equiv \hat{P}_i \cdot \hat{n}$, on the number of local Sr at 10 K.

Sr is more accessible to Ti and subsequently more effective at increasing its polarization when Sr and Ti are closer. Additionally, the multi-peak structure for $n_{\text{Sr}} \geq 1$ in Figure 6(a) can be rationalized by the fact that, for different Sr-Ti distances, the $|P_i|$ distribution is centered at different values. It can also be seen in Figure 5(a) that Ti shifts to smaller displacements with a broader distribution at higher temperatures. The decrease in the mean displacement *vs.* temperature is consistent with the Landau-Ginzburg-Devonshire theory of

first-order ferroelectric-paraelectric phase transitions.^{44–46} The structural phase transitions of BST also contribute to this decrease by suppressing components of the displacement. On the other hand, the increase in the standard deviation of the Ti displacement magnitude is due to thermal randomization in the presence of disorder. Despite the mean decrease, the distribution remains centered at non-zero displacements even in the paraelectric phase. This suggests that the ferroelectric-paraelectric phase transition of Ba-rich BST has order-disorder character.

The individual phase transitions of Ba-rich BST can be seen more clearly in Figure 5(b), which plots the distribution of the Ti displacement components against temperature. The x , y , and z components are shaded red, yellow, and blue, respectively. For temperatures below 100 K, the three distributions are superimposed, resulting in a single Gaussian (shaded purple). At 100 K, there is a rhombohedral to orthorhombic phase transition that zeroes the mean and flattens the distribution of the z component (shaded blue). The same thing happens to the remaining non-zero components at the higher-temperature phase transitions, *i.e.* orthorhombic-tetragonal at 110 K and tetragonal-cubic (ferroelectric-paraelectric) at 130 K. This plateauing of the distribution is characteristic of simultaneously order-disorder and displacive phase transitions.⁶ Therefore, the phase transitions of Ba-rich BST exhibit mixed order-disorder and displacive character, which is quite similar to pure BTO.⁶

The distribution of the Ti displacement magnitude for Sr-rich BST is plotted in Figure 5(c). At low temperatures (10 K), the peak of the distribution is located at 0.12 Å, which is smaller than those for Ba-rich BST (0.17 Å and 0.20 Å). For Sr-rich BST, the lattice constant is primarily determined by the ionic radius of Sr, which is smaller than that of Ba; this decrease in the lattice constant leads to a reduction in free volume and a suppression of the Ti displacements. The distribution of the Ti displacement components *vs.* temperature (see Figure 5(d)) show a change in the character of the ferroelectric-paraelectric phase transition that is due to the high concentration of Sr. At low temperatures (10 K), nearly all of the Ti displacements are directed along [111] (shaded purple). There are some antiparallel displacements, however, as indicated by the small peak at -0.06 Å, which suggests that the orientational correlation between dipoles is weakened by the presence of Sr. As the temperature increases (20 K < T < 40 K), the height of the antiparallel peak increases, revealing that the character of the ferroelectric-paraelectric phase transition is predominantly order-disorder. We should also emphasize that, at 40 K, unit cells resembling all three po-

lar phases (rhombohedral (shaded purple), orthorhombic (shaded orange), and tetragonal (shaded blue)) coexist, but due to the lack of strong correlation between dipoles, no single polar phase dominates. At 50 K, the two peaks have equal height, revealing an order-disorder nonpolar state. As the temperature increases further ($T > 50$ K), the value of the distribution at zero displacement begins to rise, indicating the appearance of displacive character in the phase transition.

In order to analyze the effect of n_{Sr} on the orientation correlation of Ti dipoles, we return to the case of Ba-rich BST, as it allows us to quantify the effect of individual Sr^{2+} cations. Here, we define the orientational correlation of the Ti dipole as

$$C_i \equiv \hat{P}_i \cdot \hat{n} \quad (12)$$

where \hat{P}_i is the local polarization direction, and \hat{n} is the [111] direction. Figure 6(d) shows that as n_{Sr} is increased from 0 to 4, the median C_i decreases from 0.726 to 0.659 at 100 K, *i.e.* the rhombohedral-orthorhombic phase transition temperature. Consistent with the decrease in the median C_i , the distribution also shows more dipoles far from [111]. These features suggest that Sr weakens Ti dipole correlations. The extent of C_i reduction depends monotonically on n_{Sr} . For all n_{Sr} , there are a few Ti that are antiparallel to [111], as indicated by the thin but nonzero distributions at negative C_i . These Ti have undergone thermally-induced, local polarization switching due to the rhombohedral-orthorhombic phase transition. C_i analysis enriches our view of the dipolar structure and influence of Sr on Ti by providing quantitative insights about the role of Sr doping in dipole scattering; we observe antiparallel-oriented dipoles for all numbers of local Sr, and a significant weakening of the dipole correlation for $n_{\text{Sr}} > 3$.

IV. CONCLUSIONS

In conclusion, we have developed a robust interatomic potential for BST based on the bond valence method. This potential enables accurate and efficient large-scale molecular dynamics simulations of ferroelectric alloy phenomena at the atomistic level. Here, we examine the temperature and composition dependence of the lattice parameters, Ti displacements, and polarization, and achieve excellent correspondence with experiment. Additionally, our BST potential is transferable in the sense that the parameters for each element are taken

from potentials for other materials that contain the same elements, namely BTO and STO. Such transferability facilitates the construction of potentials for complex perovskite alloy families. Due to the atomistic nature of this potential, we are able to investigate the temperature dependence of the local dipole distributions for both Ba-rich and Sr-rich BST. We discover that the ferroelectric-paraelectric phase transition character of BTO does not change significantly upon 10% Sr doping. However, in Sr-rich BST, the character of the phase transition is order-disorder at low temperatures, due to the Sr-induced weakening of dipole correlations, with displacive character emerging only at higher temperatures. Looking forward, alloy BVMD potentials not only enable the prediction of macroscopic (lattice constants, polarization, structure phase transitions, and their temperatures) and microscopic (Ti displacements) physical properties of technologically important ferroelectric perovskite alloys such as BST, BZT, PZT, and PMN-PT but also the nanoscale design of new materials via compositional tuning and heterostructure/superlattice engineering.⁴⁷⁻⁶³

ACKNOWLEDGEMENTS

R.B.W. and Y.Q. acknowledge support from the U.S. Office of Naval Research, under Grant No. N00014-17-1-2574. A.M.R. acknowledges support from the DOE Office of Basic Energy Sciences, under Grant No. DE-FG02-07ER46431. The authors also acknowledge computational support from the High-Performance Computing Modernization Office and the National Energy Research Scientific Computing Center.

-
- ¹ V. R. Cooper, I. Grinberg, and A. M. Rappe, *AIP Conf. Proc.*, **220** (2003).
 - ² Y.-H. Shin, V. R. Cooper, I. Grinberg, and A. M. Rappe, *Phys. Rev. B* **71**, 054104 (2005).
 - ³ Y.-H. Shin, B.-J. Lee, and A. M. Rappe, *J. Korean Phys. Soc.* **52**, 1206 (2008).
 - ⁴ S. Liu, I. Grinberg, and A. M. Rappe, *J. Physics.: Condens. Matter* **25**, 102202 (2013).
 - ⁵ S. Liu, I. Grinberg, H. Takenaka, and A. M. Rappe, *Phys. Rev. B* **88**, 104102 (2013).
 - ⁶ Y. Qi, S. Liu, I. Grinberg, and A. M. Rappe, *Phys. Rev. B* **94**, 134308 (2016).
 - ⁷ I. Grinberg, V. R. Cooper, and A. M. Rappe, *Nature* **419**, 909 (2002).
 - ⁸ H. Takenaka, I. Grinberg, and A. M. Rappe, *Physical Review Letters* **110**, 147602 (2013).
 - ⁹ H. Takenaka, I. Grinberg, S. Liu, and A. M. Rappe, *Nature* **546**, 391 (2017).

- ¹⁰ H. Takenaka, I. Grinberg, and A. M. Rappe, *Nature Materials* **17**, 657 (2018).
- ¹¹ J. Kim, H. Takenaka, Y. Qi, A. R. Damodaran, A. Fernandez, R. Gao, M. R. McCarter, S. Saremi, L. Chung, A. M. Rappe, *et al.*, *Adv. Mater.*, 1901060 (2019).
- ¹² I. Brown and R. Shannon, *Acta Crystallogr. A* **29**, 266 (1973).
- ¹³ I. Brown and K. K. Wu, *Acta Crystallogr. B* **32**, 1957 (1976).
- ¹⁴ Y.-H. Shin, J.-Y. Son, B.-J. Lee, I. Grinberg, and A. M. Rappe, *J. Phys.: Condens. Matter* **20**, 015224 (2008).
- ¹⁵ I. D. Brown, *Chem. Rev.* **109**, 6858 (2009).
- ¹⁶ D. G. Pettifor, I. I. Oleinik, D. Nguyen-Manh, and V. Vitek, *Comp. Mat. Sci.* **23**, 33 (2002).
- ¹⁷ M. Finnis and J. Sinclair, *Philos. Mag. A* **50**, 45 (1984).
- ¹⁸ M. A. Harvey, S. Baggio, and R. Baggio, *Acta Crystallogr. B* **62**, 1038 (2006).
- ¹⁹ Y.-H. Shin, I. Grinberg, I.-W. Chen, and A. M. Rappe, *Nature* **449**, 881 (2007).
- ²⁰ S. Liu, I. Grinberg, and A. M. Rappe, *Nature* **534**, 360 (2016).
- ²¹ H. Lu, S. Liu, Z. Ye, S. Yasui, H. Funakubo, A. M. Rappe, and A. Gruverman, *Appl. Phys. Lett.* **110**, 222903 (2017).
- ²² F. Chen, J. Goodfellow, S. Liu, I. Grinberg, M. C. Hoffmann, A. R. Damodaran, Y. Zhu, P. Zalden, X. Zhang, I. Takeuchi, A. M. Rappe, L. W. Martin, H. Wen, and A. M. Lindenberg, *Adv. Mater.* **27**, 6371 (2015).
- ²³ P. Agrawal, M. Campanini, A. Rappe, S. Liu, V. Grillo, C. Hébert, R. Erni, D. Passerone, and M. D. Rossell, *Phys. Rev. Mater.* **3**, 034410 (2019).
- ²⁴ P. Hohenberg and W. Kohn, *Phys. Rev.* **136**, B864 (1964).
- ²⁵ W. Kohn and L. J. Sham, *Phys. Rev.* **140**, A1133 (1965).
- ²⁶ P. Giannozzi, S. Baroni, N. Bonini, M. Calandra, R. Car, C. Cavazzoni, D. Ceresoli, G. L. Chiarotti, M. Cococcioni, I. Dabo, A. D. Corso, S. de Gironcoli, S. Fabris, G. Fratesi, R. Gebauer, U. Gerstmann, C. Gougoussis, A. Kokalj, M. Lazzeri, L. Martin-Samos, N. Marzari, F. Mauri, R. Mazzarello, S. Paolini, A. Pasquarello, L. Paulatto, C. Sbraccia, S. Scandolo, G. Sclauzero, A. P. Seitsonen, A. Smogunov, P. Umari, and R. M. Wentzcovitch, *J. Phys.: Condens. Matter* **21**, 395502 (2009).
- ²⁷ N. J. Ramer and A. M. Rappe, *Phys. Rev. B* **59**, 12471 (1999).
- ²⁸ A. M. Rappe, K. M. Rabe, E. Kaxiras, and J. D. Joannopoulos, *Phys. Rev. B Rapid Comm.* **41**, 1227 (1990).

- ²⁹ J. P. Perdew, A. Ruzsinszky, G. I. Csonka, O. A. Vydrov, G. E. Scuseria, L. A. Constantin, X. Zhou, and K. Burke, *Phys. Rev. Lett.* **100**, 136406 (2008).
- ³⁰ S. Plimpton, *J. Comp. Phys.* **117**, 1 (1995).
- ³¹ S. Nosé, *J. Chem. Phys.* **81**, 511 (1984).
- ³² S. Nosé, *Mol. Phys.* **52**, 255 (1984).
- ³³ W. G. Hoover, *Phys. Rev. A* **31**, 1695 (1985).
- ³⁴ M. Parrinello and A. Rahman, *Phys. Rev. Lett.* **45**, 1196 (1980).
- ³⁵ M. Parrinello and A. Rahman, *J. Appl. Phys.* **52**, 7182 (1981).
- ³⁶ V. Lemanov, E. Smirnova, P. Syrnikov, and E. Tarakanov, *Phys. Rev. B* **54**, 3151 (1996).
- ³⁷ C. Menoret, J. Kiat, B. Dkhil, M. Dunlop, H. Dammak, and O. Hernandez, *Phys. Rev. B* **65**, 224104 (2002).
- ³⁸ M. Acosta, N. Novak, V. Rojas, S. Patel, R. Vaish, J. Koruza, G. Rossetti Jr, and J. Rödel, *Appl. Phys. Rev.* **4**, 041305 (2017).
- ³⁹ S. Tinte, M. G. Stachiotti, S. R. Phillpot, M. Sepiarsky, D. Wolf, and R. L. Migoni, *J. Phys.: Condens. Matter* **16**, 3495 (2004).
- ⁴⁰ L. Walizer, S. Lisenkov, and L. Bellaiche, *Physical Review B* **73**, 144105 (2006).
- ⁴¹ T. Nishimatsu, A. Gruenebohm, U. V. Waghmare, and M. Kubo, *Journal of the Physical Society of Japan* **85**, 114714 (2016).
- ⁴² S. Tinte, M. G. Stachiotti, M. Sepiarsky, R. L. Migoni, and C. O. Rodriguez, *J. Phys.: Condens. Matter* **11**, 9679 (1999).
- ⁴³ P. Ghosez, X. Gonze, P. Lambin, and J.-P. Michenaud, *Phys. Rev. B* **51**, 6765 (1995).
- ⁴⁴ L. Landau, *Phys. Z. Sowjetunion* **11**, 26 (1937).
- ⁴⁵ A. F. Devonshire, *The London, Edinburgh, and Dublin Philosophical Magazine and Journal of Science* **40**, 1040 (1949).
- ⁴⁶ V. Ginzburg and L. Landau, *J. Exp. Theor. Phys. USSR* **20**, 1064 (1950).
- ⁴⁷ P. Ghosez, D. Desquesnes, X. Gonze, and K. Rabe, in *AIP Conf. Proc.*, Vol. 535 (AIP, 2000) pp. 102–110.
- ⁴⁸ H. Li, H. Zheng, L. Salamanca-Riba, R. Ramesh, I. Naumov, and K. Rabe, *Appl. Phys. Lett.* **81**, 4398 (2002).
- ⁴⁹ K. Johnston, X. Huang, J. B. Neaton, and K. M. Rabe, *Phys. Rev. B* **71**, 100103 (2005).

- ⁵⁰ D. L. Kaiser, M. D. Vaudin, L. D. Rotter, J. E. Bonevich, I. Levin, J. T. Armstrong, A. L. Roytburd, and D. G. Schlom, *J. Mater. Res.* **14**, 4657 (1999).
- ⁵¹ W. Tian, J. Jiang, X. Pan, J. Haeni, Y. Li, L. Chen, D. Schlom, J. Neaton, K. Rabe, and Q. Jia, *Appl. Phys. Lett.* **89**, 092905 (2006).
- ⁵² Y. Li, S. Y. Hu, D. Tenne, A. Soukiassian, D. Schlom, L. Chen, X. Xi, K. J. Choi, C. Eom, A. Saxena, *et al.*, *Appl. Phys. Lett.* **91**, 252904 (2007).
- ⁵³ A. Bruchhausen, A. Fainstein, A. Soukiassian, D. Schlom, X. Xi, M. Bernhagen, P. Reiche, and R. Uecker, *Phys. Rev. Lett.* **101**, 197402 (2008).
- ⁵⁴ K. Kathan-Galipeau, P. Wu, Y. Li, L.-Q. Chen, A. Soukiassian, X. Xi, D. G. Schlom, and D. A. Bonnell, *ACS Nano* **5**, 640 (2010).
- ⁵⁵ A. Bruchhausen, A. Fainstein, S. Tinte, A. Soukiassian, D. Schlom, and X. Xi, *Chin. J. Phys.* **49**, 159 (2011).
- ⁵⁶ K. Kathan-Galipeau, P. Wu, Y. Li, L.-Q. Chen, A. Soukiassian, Y. Zhu, D. A. Muller, X. Xi, D. G. Schlom, and D. A. Bonnell, *J. Appl. Phys.* **112**, 052011 (2012).
- ⁵⁷ C.-H. Lee, N. D. Orloff, T. Birol, Y. Zhu, V. Goian, E. Rocas, R. Haislmaier, E. Vlahos, J. A. Mundy, L. F. Kourkoutis, *et al.*, *Nature* **502**, 532 (2013).
- ⁵⁸ G. Subramanyam, M. W. Cole, N. X. Sun, T. S. Kalkur, N. M. Sbrockey, G. S. Tompa, X. Guo, C. Chen, S. Alpay, G. Rossetti Jr, *et al.*, *Journal of applied physics* **114**, 13.1 (2013).
- ⁵⁹ V. Železný, A. Soukiassian, D. Schlom, and X. Xi, *J. Appl. Phys.* **115**, 184102 (2014).
- ⁶⁰ V. Železný, A. Soukiassian, X. Xi, and D. G. Schlom, *Phase Transitions* **87**, 929 (2014).
- ⁶¹ P. Wu, X. Ma, Y. Li, C.-B. Eom, D. G. Schlom, V. Gopalan, and L.-Q. Chen, *Appl. Phys. Lett.* **107**, 122906 (2015).
- ⁶² V. Železný, O. Caha, A. Soukiassian, D. Schlom, and X. Xi, *Phys. Rev. B.* **95**, 214110 (2017).
- ⁶³ X. Wei, A. L. Vasiliev, and N. P. Padture, *J. Mater. Res.* **20**, 2140 (2005).

Supplemental Material

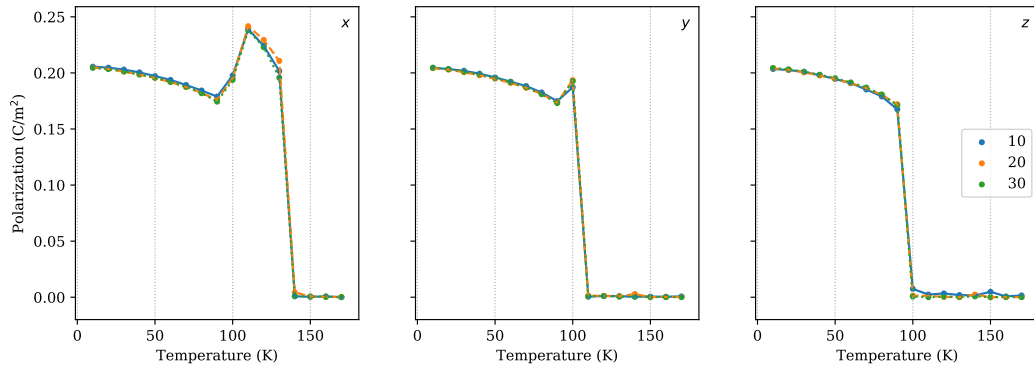


FIG. S1. Temperature dependence of the polarization components of BST for different supercell sizes: $10 \times 10 \times 10$, $20 \times 20 \times 20$, and $30 \times 30 \times 30$.